

Article

Free-Space Quantum Teleportation with Orbital Angular Momentum Multiplexed Continuous Variable Entanglement

Xinchao Ruan ¹, Hang Zhang ¹, Wenqi Peng ¹, Hui Xian ¹, Yiwu Zhu ¹, Wei Zhao ^{2,3,*} and Sha Xiong ^{1,*}¹ School of Automation, Central South University, Changsha 410083, China² Key Laboratory of Computing Power Network and Information Security, Ministry of Education, Shandong Computer Science Center (National Supercomputer Center in Jinan), Qilu University of Technology (Shandong Academy of Sciences), Jinan 250316, China³ Shandong Provincial Key Laboratory of Computer Networks, Shandong Fundamental Research Center for Computer Science, Jinan 250353, China

* Correspondence: zhaow@sdas.org (W.Z.); xiongsha@csu.edu.cn (S.X.)

Abstract: Quantum teleportation is one of the fundamental primitives of quantum cryptography. In order to achieve a wider range of high-capacity information transfer, we propose a free-space quantum teleportation (QT) protocol with orbital angular momentum (OAM) multiplexed continuous variable (CV) entangled states. The preparation of the entangled states is accomplished by the spontaneous four-wave mixing (SFWM) process occurring in a hot ⁸⁵Rb vapor cell, and the mode selection for the Bell-state measurement is achieved by employing the balanced homodyne detection technique. The fidelity of teleporting EPR entangled states carrying different topological charges via a Kolmogorov-type atmospheric turbulence channel is derived, and the superiority of enhancing the system channel capacity via OAM multiplexing is demonstrated. Our work provides a feasible scheme to implement high-capacity quantum communication in atmospheric environments.

Keywords: quantum teleportation; orbital angular momentum; free space; continuous variable**MSC:** 81P94; 81P45

Citation: Ruan, X.; Zhang, H.; Peng, W.; Xian, H.; Zhu, Y.; Zhao, W.; Xiong, S. Free-Space Quantum Teleportation with Orbital Angular Momentum Multiplexed Continuous Variable Entanglement. *Mathematics* **2023**, *11*, 3209. <https://doi.org/10.3390/math11143209>

Academic Editor: Carsten Schneider

Received: 10 June 2023

Revised: 17 July 2023

Accepted: 18 July 2023

Published: 21 July 2023



Copyright: © 2023 by the authors. Licensee MDPI, Basel, Switzerland. This article is an open access article distributed under the terms and conditions of the Creative Commons Attribution (CC BY) license (<https://creativecommons.org/licenses/by/4.0/>).

1. Introduction

Quantum teleportation (QT) technology enables the transfer of information without the transmission of unknown quantum states, with the aid of quantum entangled states pre-shared between the communicating parties and classical communication. The first QT protocol was proposed by Bennett et al. [1], and, since then, various investigations on theoretical analysis and experimental implementation have been developed [2–4]. In the initial period, single-photon qubits were chosen as the physical carrier for QT to enable information transmission over long distances, benefiting from the relative simplicity of the generation system and negligible decoherence to noisy environments. For instance, Marcikic et al. reported an experimental demonstration of probabilistic QT over 2 km of standard telecommunication fiber [5]. Yin and Ma experimentally confirmed QT in two free-space optical links over 100 km magnitude [6,7]. Ren et al. reported QT of independent single-photon qubits from a ground observatory to a low-Earth-orbit satellite over distances of up to 1400 km [8]. Despite the tremendous progress that has been made in QT with discrete variables, all of these are probabilistic, hindering the instantaneous transfer of quantum states without post-selection [9].

To overcome this obstacle, the QT protocol with continuous variable (CV) entangled states was proposed, in which the unknown quantum states can be transferred unconditionally and deterministically [10,11]. The transfer and retrieval of the quantum states with this method in fiber, seawater, atmosphere, and even satellite-ground channels have been verified theoretically or experimentally. However, most of the current research has

focused on improving the fidelity of the teleported quantum state and increasing the scale of communication distance. Typically, non-Gaussian entangled sources, arising from operations such as photon addition and subtraction [12,13], photon catalysis [14], and noiseless quantum amplification [15–18], were used in CVQT protocols to improve system fidelity. Otherwise, non-traditional coherent state sources such as discrete variable sources [19,20], spin coherent states [21], and thermal states [22] were also employed to achieve this goal. In terms of the scale of communication distance, Huo et al. realized the first experimental implementation of deterministic teleportation of optical modes over a fiber channel of 6.0 km [9]. Zhao et al. experimentally implemented a real-time deterministic quantum teleportation over 10 km of single optical fiber channel [23]. On this basis, Wen et al. proposed to further increase the secure communication distance while improving the system fidelity with methods such as photon catalysis and noiseless linear amplification [14,15]. Similarly, Wu and Xu et al. proposed that the fidelity and transmission distance of CVQT systems in underwater and turbulent atmospheric channels can be improved using noiseless linear amplifier, respectively [17,18]. Furthermore, Zuo et al. theoretically demonstrated the realisability of the CVQT protocol in a ground-to-satellite uplink, thereby extending the transmission distance to the hundreds of kilometres scale [24].

With respect to the information transmission capacity, which is also a very central element for the practical application of the CVQT protocol, it is rarely mentioned. Up to now, only Liu and Wu have proposed, respectively, that the use of OAM multiplexing and multi-channel multiplexing in an optical frequency comb system can achieve CVQT over fiber channels, which can ensure the enhancement of information transmission capacity [25,26]. On the other hand, to construct an all-around quantum communication network, quantum communication based on atmospheric channels is indispensable. Considering the more complex situation of turbulent atmosphere, whether these existing methods can still establish superiority in terms of fidelity and channel capacity has not been confirmed. Therefore, in our work, we propose a CV-QT protocol with orbital angular momentum (OAM) multiplexed Einstein–Podolsky–Rosen (EPR) entangled states in a free-space atmospheric environment. The entangled states are generated from the double- Λ configuration spontaneous four-wave mixing (SFWM) process in a hot ^{85}Rb vapor cell, and the mode selection for the Bell-state measurement is ensured by the balanced homodyne detection technique. Based on the properties of the atmospheric turbulence channel with the Kolmogorov model and the propagation characteristics of the OAM state, we construct the crosstalk matrix of the transmitted OAM states and the density matrix of the detected OAM states, and, on this basis, we derive the fidelity of the QT protocol and establish the dominant region of the proposed scheme in terms of fidelity with respect to transmission distance and atmospheric turbulence intensity by simulations. In addition, to illustrate the superiority of OAM multiplexing in enhancing the channel capacity, we also simulate the channel capacity versus transmission distance and turbulence intensity for different number of OAM states multiplexed under weak turbulence, thus confirming the significant advantage of OAM multiplexing in enhancing the channel capacity.

The paper is organized as follows. In Section 2, the scheme of the free-space QT with OAM multiplexed CV EPR states is described, and the properties of the atmospheric turbulence channel and the propagation characteristics of the OAM multiplexed EPR state are analysed. In Section 3, the fidelity of the protocol is derived and the channel capacity is simulated. Finally, the conclusion is drawn in Section 4.

2. Free-Space QT with OAM Multiplexed CV EPR States

2.1. Scheme Description

The scheme of the free-space QT protocol with OAM multiplexed CV entangled states is shown in Figure 1, and the detailed implementation process can be described as follows.

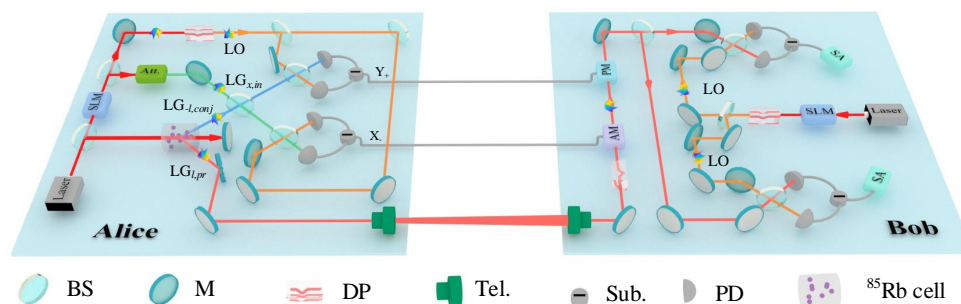


Figure 1. Schematic diagrams of the free-space QT with OAM multiplexed CV entangled states. BS, beam splitter; M, mirror; DP, Dove prism; Sub., subtractor; PD, photo detector; Tel., telescope; SLM, spatial light modulator; Att., attenuator; AM, amplitude modulator; PM, phase modulator; SA, spectrum analyser.

Preparation. At Alice’s side, a strong Gaussian beam is emitted from a cavity stabilized Ti:sapphire laser and divided into two parts by a beam splitter (BS). The stronger part is modulated by a spatial light modulator (SLM) and then split into two parts by another BS, one of which is attenuated by an attenuator for preparing the spatial-phase-randomized vortex beam $LG_{x,in}$ with OAM mode $|\psi_{x,in}\rangle$ as the unknown input state, and the other is transferred to the opposite OAM mode by a Dove prism (DP) to serve as the local oscillator (LO). The weaker part is seeded into a warm ^{85}Rb vapor cell, serving as the pump beam of the SFWM process in the cell for generating OAM multiplexed EPR entangled pairs $|\psi_{l,pr}\rangle$ and $|\psi_{-l,conj}\rangle$ [27], whose specific preparation process is described in Appendix A.

Distribution. After the SFWM process, the mode $|\psi_{-l,conj}\rangle$ of the conjugate beam is retained by Alice for Bell measurement with the unknown input state $|\psi_{x,in}\rangle$, while the mode $|\psi_{l,pr}\rangle$ of the probe beam is distributed to Bob through a free-space atmospheric channel. In cylindrical coordinates, the mode $|\psi_{l,pr}\rangle$ has the general form [28–31]

$$\varphi_{p,l}(r, \theta, z) = R_{p,l}(r, z) \frac{\exp(i l \theta)}{\sqrt{2\pi}}, \tag{1}$$

where r and θ are the radial and azimuthal coordinates, respectively, z is the propagation distance, p and l are the radial and angular mode numbers, respectively, and $R_{p,l}(r, z)$ is the radial profile. In our work, the entangled source generated from the SFWM process is considered as a Laguerre–Gaussian (LG) beam, whose radial profile is a Laguerre–Gauss function, namely

$$R_{p,l}(r, z) = \sqrt{\frac{4p!}{(p + |l|)!} \frac{1}{\omega(z)} \left[\frac{r\sqrt{2}}{\omega(z)} \right]^{|l|}} \exp\left[\frac{-r^2}{\omega^2(z)} \right] L_p^{|l|} \left(\frac{2r^2}{\omega^2(z)} \right) \times \exp\left[\frac{-ikr^2z}{2(z^2 + z_R^2)} \right] \exp\left[i(2p + |l| + 1)\tan^{-1} \frac{z}{z_R} \right], \tag{2}$$

where $\omega(z) = \omega_0 \sqrt{1 + (z/z_R)^2}$, ω_0 is the radius of the zero-order Gaussian beam at the waist, $z_R = \pi\omega_0^2/\lambda$ is the Rayleigh range, λ is the wavelength, $k = 2\pi/\lambda$ is the wave number, and $L_p^l(\cdot)$ is the generalized Laguerre polynomial. For the sake of simplicity, we only consider the case of $p = 0$.

Bell Measurement. Alice interferes the unknown input state $|\psi_{x,in}\rangle$ with the conjugate modes $|\psi_{-l,conj}\rangle$ via a balanced BS, resulting in

$$\begin{aligned}
 C &= (|\psi_{x,in}\rangle - |\psi_{-l,conj}\rangle) / \sqrt{2}, \\
 D &= i(|\psi_{x,in}\rangle + |\psi_{-l,conj}\rangle) / \sqrt{2},
 \end{aligned}
 \tag{3}$$

as the signal field for CV Bell measurement with a pair of balanced homodyne detectors (BHDs). According to existing research, only the signal field carrying the opposite topological charge with the LO can be detected [27], as detailed in Appendix B. Therefore, only the output modes C and D of the interference field carrying a single topological charge can be measured, which implies that there is a mode in the conjugate field with the same topological charge as the unknown input state, which can be generalized to $-l$. The LO for BHDs originates from the SLM modulated beam being transferred from the LO_{-l} mode to the LO_l mode by a Dove prism. Thus, the joint measurement has the result of

$$\begin{aligned}
 \hat{X}_- &= (\hat{X}_{-l,in} - \hat{X}_{-l,conj}) / \sqrt{2}, \\
 \hat{Y}_+ &= (\hat{Y}_{-l,in} + \hat{Y}_{-l,conj}) / \sqrt{2},
 \end{aligned}
 \tag{4}$$

and they are transmitted to Bob through the classical channel.

Displacement. The mode $|\psi_{l,pr}\rangle$ arriving at Bob’s side is transferred to $|\psi_{-l,pr}\rangle$ by another Dove prism and then modulated by an amplitude modulator (AM) and a phase modulator (PM) excited by the measured quadratures \hat{X}_- and \hat{Y}_+ , respectively. Therefore, after the OAM transformation and coherent displacement operation, the probe state becomes

$$\begin{aligned}
 \hat{X}_{l,pr} &\rightarrow \hat{X}_{-l,pr} + \sqrt{2}\hat{X}_-, \\
 \hat{Y}_{l,pr} &\rightarrow \hat{Y}_{-l,pr} + \sqrt{2}\hat{Y}_+.
 \end{aligned}
 \tag{5}$$

In the limit of strong squeezing, the prepared EPR pairs have the following property [32]:

$$\begin{aligned}
 \hat{X}_{l,pr} - \hat{X}_{-l,conj} &= 0, \\
 \hat{Y}_{l,pr} + \hat{Y}_{-l,conj} &= 0.
 \end{aligned}
 \tag{6}$$

Assuming that the Dove prism is perfect, then the intensity and phase quadratures of the quantum state remains constant before and after the OAM mode transformation, so we have

$$\hat{X}_{-l,pr} = \hat{X}_{l,pr}, \hat{Y}_{-l,pr} = \hat{Y}_{l,pr}.
 \tag{7}$$

Combining Equations (4)–(7), Bob can retrieve the input state by two balanced homodyne detections. The locally generated spatial mode-matched LOs used here are the same as those in the Bell measurement, which is ensured by the same modulation information acting on the SLMs.

2.2. Properties of the Atmospheric Turbulence Channel

In our scheme, the probe mode $|\psi_{l,pr}\rangle$ is distributed to Bob via an atmospheric turbulence channel, which is considered as a horizontal link. For simplicity, we assume that the atmospheric turbulence satisfies local uniform isotropy at short distances, in which case the Kolmogorov model can be used to describe the atmospheric turbulence with a power spectrum of [33]:

$$\Phi(\kappa) = 0.033C_n^2\kappa^{-11/3},
 \tag{8}$$

where C_n^2 is the atmospheric refractive index structure parameter, and $\kappa \in [2\pi/l_{out}, 2\pi/l_{in}]$ with the outer scale parameter l_{out} and the inner scale parameter l_{in} is the magnitude of the three-dimensional coordinate vector in the Fourier domain. The details regarding the Kolmogorov turbulence model are described in Appendix C. Therefore, the output state after the channel can be derived by mapping $I_A \otimes M_B$ to the initially prepared state $|\Psi\rangle_{AB}$, where I is the identity operator and $M = \sum_{m,n} \sqrt{P(m|n)} |\psi_{m,pr}\rangle \langle \psi_{n,pr}|$ is the turbulent

channel operator that can be constructed via the transition probabilities $P(m|n)$ from probe state $|\psi_{n,pr}\rangle$ to $|\psi_{m,pr}\rangle$ [34]. According to existing research, $P(m|n)$ can be calculated as [35,36]

$$P(m|n) = \frac{1}{\pi} \int_0^1 \rho d\rho \int_0^{2\pi} \exp[-6.88 \times 2^{\frac{2}{3}} (\frac{r}{r_0} \sin \frac{\theta}{2})^{5/3} - i(m-n)\theta] d\theta, \tag{9}$$

where $\rho = r/R$ with the receiving aperture radius R and radial radius $r = \sqrt{|n| + 1} \omega_z$, in which $\omega_z = \omega_0 \sqrt{1 + (z/Z_R)^2}$, $Z_R = \pi \omega_0^2 / \lambda$, ω_0 is the radius of the zero-order Gaussian beam at the waist, λ is the wavelength, and z is the propagation distance; $r_0 = 0.185(\lambda^2 / C_n^2 z)^{3/5}$ is the Fried parameter, and θ is the difference of azimuth coefficients before and after divergence.

The atmospheric turbulence channel can be characterized by the effective transmittance and the channel excess noise. The effective transmittance of different OAM states propagating in the atmospheric channel can be derived from the correct propagation probability of the initial mode detected by the receiver, namely [37,38]

$$T(l, C_n^2, z) = e^{-\alpha(\lambda)z} \cdot P(n|n), \tag{10}$$

where $P(n|n)$ is the probability of the initial mode detected by the receiver, and $\alpha(\lambda)$ is the link attenuation coefficient with [39,40]:

$$\alpha(\lambda) = \alpha_{sca}^{aer}(\lambda) + \alpha_{abs}^{aer}(\lambda) + \alpha_{sca}^{mol}(\lambda) + \alpha_{abs}^{mol}(\lambda), \tag{11}$$

where $\alpha_{sca}^{aer}(\lambda)$ is the aerosol scattering coefficient, $\alpha_{abs}^{aer}(\lambda)$ is the aerosol absorption coefficient, $\alpha_{sca}^{mol}(\lambda)$ is the molecular scattering coefficient, and $\alpha_{abs}^{mol}(\lambda)$ is the molecular absorption coefficient. The attenuation coefficient varies under different conditions, and the typical values are shown in Table 1. In our scheme, the channel condition is assumed to be clear air, in which case the attenuation coefficient can be 0.1 km^{-1} .

Table 1. The typical attenuation coefficient under different conditions.

Condition	Clear Air	Haze	Fog	Dense Fog
Value (km^{-1})	≈ 0.1	≈ 1.0	≥ 10	≈ 391

The channel excess noise may originate from multiple sources, such as from imperfect modulation, intensity fluctuations of the used lasers, background light, and so on [41,42]. In our work, we will focus on the crosstalk noise among different OAM modes caused by the atmospheric turbulence, which can be expressed as [38]

$$\epsilon_{cross} = \frac{\tau P_{cross}}{\hbar v_c}, \tag{12}$$

where $\tau = 1 \text{ ns}$ is the effective sampling period, \hbar is the Planck constant, v_c is the frequency of the noise photons satisfying $\hbar v_c = 1.28 \times 10^{-19} \text{ J}$, and P_{cross} is the noise power induced by crosstalk with

$$P_{cross}(m) = \sum_{n \neq m} P(m|n) \cdot P_{in}, \tag{13}$$

where $P(m|n)$ is the crosstalk probability of the other modes n to the mode m , and it can be calculated by Equation (9). Additionally, $P_{in} = -85.9 \text{ dBm}$ is the input power of the vortex beam. Therefore, the channel excess noise refers to the input of the channel for different OAM modes and can be expressed as

$$\epsilon = (\epsilon_{limit} + \epsilon_{cross}) / T, \tag{14}$$

where $\epsilon_{limit} = 0.01$ SNU (shot noise unit) represents the maximum value of the original excess noise of the atmospheric channel due to the relative intensity fluctuation.

Figure 2a,b show the effect of transmission distance and turbulence intensity on the transmittance and excess noise of the atmospheric channel, respectively. Without loss of generality, OAM states with the same absolute value of topological charge have the same channel transmission properties, so we take the OAM states with topological charges of 0, 1, and 2 as an example for simulation. The results show that the transmittance of the channel decreases with the increase in the transmission distance and the intensity of the atmospheric turbulence, whereas the opposite is true for the excess noise. Furthermore, the higher the topological charge number, the lower the transmittance, and the higher the excess noise.

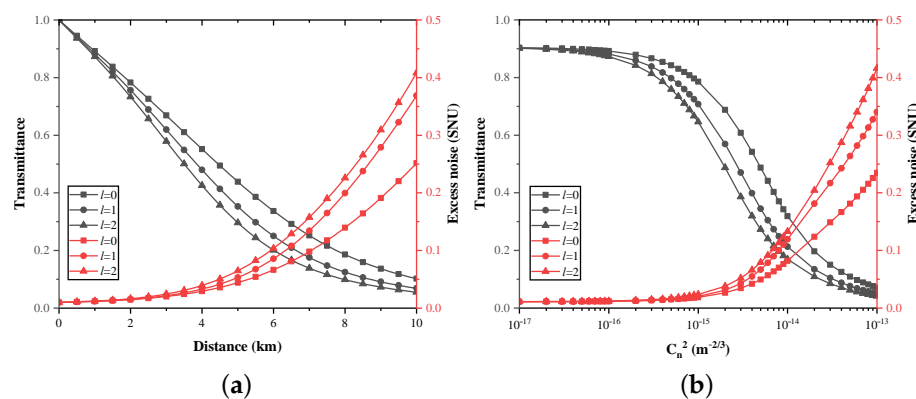


Figure 2. The properties of the atmospheric turbulence channel in terms of different OAM modes. (a) Transmittance and excess noise versus the propagation distance with $C_n^2 = 10^{-16} \text{ m}^{-2/3}$; (b) transmittance and excess noise versus the atmospheric turbulence intensity with $z = 1 \text{ km}$.

2.3. Propagation Characteristics of the OAM Multiplexed EPR State

Due to the presence of atmospheric turbulence, the probe mode of the prepared OAM multiplexed EPR entangled state is subjected to the absorption and scattering effects of the atmosphere when it is transmitted over an atmospheric channel. Absorption may lead to decoherence, rendering the quantum state damaged; scattering may lead to crosstalk of modes into the adjacent modes, making the detection of the modes inaccurate. Therefore, we need to comprehensively consider the effects of these two factors on the propagation characteristics of the OAM multiplexed EPR state.

The coherence of a quantum state is defined as the minimum distance between the quantum state and an incoherent state in the Hilbert space, and it can be quantified by relative entropy, namely [43,44]

$$C_{coh}[\hat{\rho}_l(\bar{\mathbf{x}}, \mathbf{V})] = S[\hat{\rho}_{th}(\bar{\mathbf{x}}_{th}, \mathbf{V}_{th})] - S[\hat{\rho}_l(\bar{\mathbf{x}}, \mathbf{V})], \tag{15}$$

where $S[\hat{\rho}_l(\bar{\mathbf{x}}, \mathbf{V})]$ is the von Neumann entropy of the prepared EPR entangled state $\hat{\rho}_l(\bar{\mathbf{x}}, \mathbf{V})$ with displacement $\bar{\mathbf{x}}$ and covariance matrix \mathbf{V} , $S[\hat{\rho}_{th}(\bar{\mathbf{x}}_{th}, \mathbf{V}_{th})]$ is that of a thermal state $\hat{\rho}_{th}(\bar{\mathbf{x}}_{th}, \mathbf{V}_{th})$ with displacement $\bar{\mathbf{x}}_{th}$ and covariance matrix \mathbf{V}_{th} , and they can be calculated as

$$S[\hat{\rho}_l(\bar{\mathbf{x}}, \mathbf{V})] = - \sum_{i=1}^2 \left[\frac{v_i - 1}{2} \log_2 \left(\frac{v_i - 1}{2} \right) - \frac{v_i + 1}{2} \log_2 \left(\frac{v_i + 1}{2} \right) \right],$$

$$S[\hat{\rho}_{th}(\bar{\mathbf{x}}_{th}, \mathbf{V}_{th})] = - \sum_{i=1}^2 \left[\frac{\mu_i - 1}{2} \log_2 \left(\frac{\mu_i - 1}{2} \right) - \frac{\mu_i + 1}{2} \log_2 \left(\frac{\mu_i + 1}{2} \right) \right], \tag{16}$$

where v_i and μ_i are the symplectic eigenvalues of \mathbf{V} and \mathbf{V}_{th} , respectively. The covariance matrix of the OAM multiplexed EPR entangled state after distribution in a noisy atmospheric channel is

$$\mathbf{V} = \begin{pmatrix} \mathbf{A} & \mathbf{C} \\ \mathbf{C}^T & \mathbf{B} \end{pmatrix}, \tag{17}$$

where $\mathbf{A} = [(V + V')/2]\mathbf{I}$, $\mathbf{B} = [T(V + V')/2 + (1 - T)(1 + \varepsilon)]\mathbf{I}$, $\mathbf{C} = [\sqrt{T}(V' - V)/2]\mathbf{Z}$, with $\mathbf{I} = \begin{pmatrix} 1 & 0 \\ 0 & 1 \end{pmatrix}$ and $\mathbf{Z} = \begin{pmatrix} 1 & 0 \\ 0 & -1 \end{pmatrix}$; T and ε are the transmittance and excess noise of the atmospheric channel, and V and V' are the variances of correlation and anti-correlation quadratures of the EPR entangled state, respectively.

The dependence of quantum coherence of the OAM multiplexed EPR entangled states on the transmittance under the condition of $C_n^2 = 10^{-16} \text{ m}^{-2/3}$ is shown in Figure 3. The excess noise ε varies dynamically depending on the transmittance and topological charge l , and it can be calculated jointly by Equations (10) and (14). The correlation and anti-correlation levels of the initial entangled state are about -3.3 dB and 6.1 dB , corresponding to $V = 0.47$ and $V' = 4.11$, respectively, as set in Ref. [43]. The quantum coherence of the entangled states carrying the topological charge $l = 1$ and $l = 2$ is close to that of their Gaussian counterpart with $l = 0$, and the differences that exist are mainly attributed to the fact that the OAM states carrying different topological charges are subjected to different noises on the channel. Given that the transmittance is mainly affected by the transmission distance and the intensity of atmospheric turbulence, we can further explore their effects on the coherence between the probe and conjugate modes, which are shown in Figure 4. The simulation results show that the coherence decreases with the increase in the transmission distance of the probe mode in the channel as well as with the increase in the atmospheric turbulence intensity, and the larger the topological charge l carried by the probe mode, the faster the coherence decreases, which is mainly due to the fact that it is also subjected to the larger noise perturbation. The above analysis indicates that, although the atmospheric absorption effect causes the coherence between the probe and conjugate modes to decrease, it always exists until the transmittance decreases to 0, which means that the coherence of the EPR entangled states carrying OAM decreases but does not decoherence.

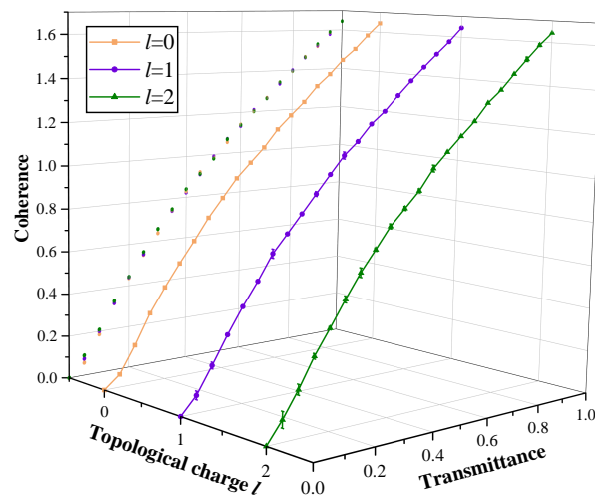


Figure 3. Dependence of quantum coherence of the OAM multiplexed EPR entangled states on the transmittance for $l = 0, l = 1$, and $l = 2$. The error bars represent the difference between the coherence of the entangled state with topological charge l and that of the Gaussian state.

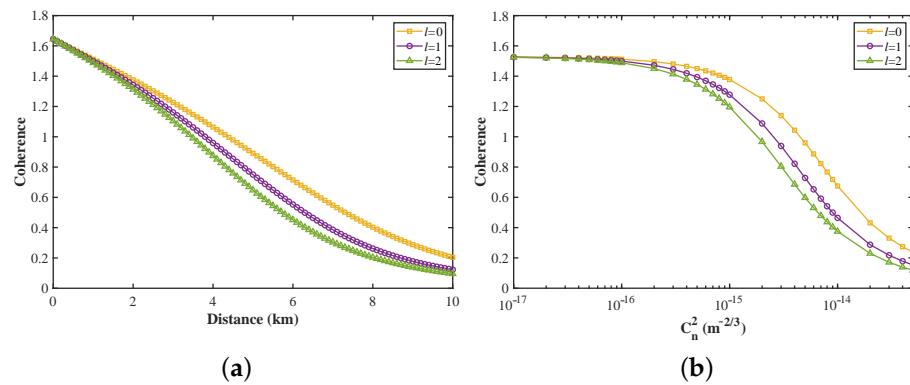


Figure 4. The effect of transmission distance and atmospheric turbulence intensity on the coherence between the probe and conjugate modes: **(a)** on the condition of $C_n^2 = 10^{-16} \text{ m}^{-2/3}$; **(b)** on the condition of $z = 1 \text{ km}$. The excess noise ϵ varies dynamically with the two variables in the subfigures.

The crosstalk probability due to the scattering effect can be calculated by Equation (9), and the corresponding crosstalk matrix is shown in Figure 5a. Here we only consider the case of $m, n \in [-4, 4]$ for simplicity. The elements on the diagonal (red bars) represent the probability that the probe mode distributed by Alice propagates correctly to Bob’s side, whereas the elements on the non-diagonal (blue bars) characterize the probability of scattering to the other modes. In the SFWM process, a series of CV EPR entangled states carrying independent topological charges are generated, which means that the prepared state is a hybrid entangled state. Each entangled pair can be mapped onto a density operator $\rho_l = |\psi_{-l,conj}\rangle\langle\psi_{l,pr}|$ by actively switching between OAM modes sequentially in time. The density matrix of this system can be expressed as [45]

$$\Gamma_{AB} = \sum_{l=1}^{\infty} \gamma_l \rho_l, \tag{18}$$

where γ_l represents the probability of post-selecting the hybrid state ρ_l . The density matrix pertaining to system related to the mode B is

$$\Gamma_B = \text{Tr}_A(\Gamma_{AB}) = \sum_{l=0}^{\infty} \frac{\gamma_l}{2} (|\psi_{l,pr}\rangle\langle\psi_{l,pr}| + |\psi_{-l,pr}\rangle\langle\psi_{-l,pr}|), \tag{19}$$

where $\text{Tr}_A(\cdot)$ is the partial trace over mode A. Furthermore, due to the presence of atmospheric turbulence disturbances, the initial mode B may be scattered into adjacent modes after transmission through the channel. Thus, the density matrix of the hybrid quantum state received by Bob can be calculated as

$$\Gamma_{B_1} = \sum_{m,n} P(m|n) (|\psi_{n,pr}\rangle\langle\psi_{n,pr}| + |\psi_{m,pr}\rangle\langle\psi_{m,pr}|), \tag{20}$$

and it can be visually represented as shown in Figure 5b, which is essentially used to characterize the detection probability of the OAM state. The basic parameter settings are listed in Table 2. The elements on the diagonal (red bars) represent the detection probability for each OAM state, which contains the correct transmission probability of the OAM state and the crosstalk probability of other modes into that mode. Similarly, the elements on the non-diagonal (blue bars) characterize the probability of scattering to the other modes.

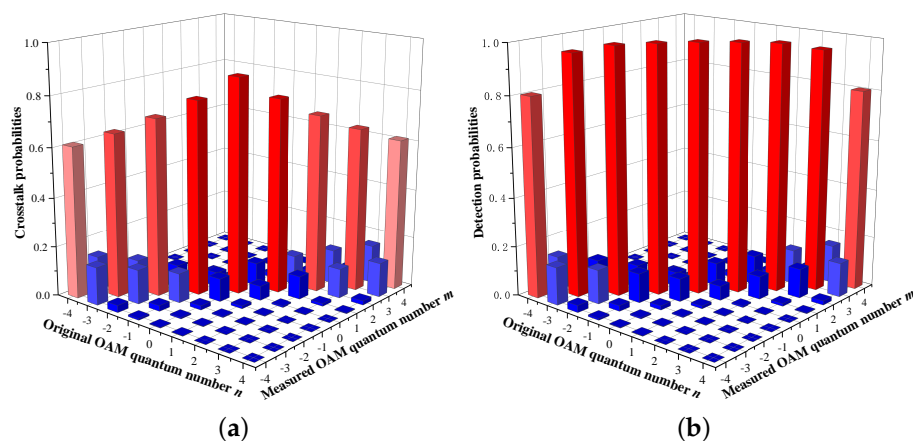


Figure 5. (a) The crosstalk matrix of the transmitted OAM states. (b) The density matrix of the detected OAM states.

Table 2. Simulation parameter setting.

Parameter	Description	Value
ω_0	radius of zero-order Gaussian beam at the waist	3 cm
λ	wavelength	1550 nm
C_n^2	atmospheric refractive index structure parameter	$10^{-15} \text{ m}^{-2/3}$
z	propagation distance	1 km

3. Performance Analysis

3.1. Fidelity

From the quantum mechanical definition, the fidelity to be measured in our scheme is a measure of the similarity between the output state $|\psi_{y,out}\rangle$ and the unknown input state $|\psi_{x,in}\rangle$. Given that three degrees of freedom—amplitude, phase, and OAM—of the quantum state are considered in our scheme, the fidelity of the unknown input state can be calculated from the product of the fidelity in terms of the three degrees of freedom. Assuming that the input state is a coherent state, the fidelity in terms of amplitude and phase quadratures can be expressed as [18,24]

$$F_{ap} = \frac{2}{3 - T + (T + 1)\cosh(2r_s) - 2\sqrt{T}\sinh(2r_s) + \varepsilon'} \tag{21}$$

where r_s is the squeezing parameter. Under the assumption that the experimental equipment is perfect, and in conjunction with the scheme we have devised, it is clear that the probe state must be correctly transmitted to Bob’s side to enable the teleportation of the unknown input state. Therefore, the calculation of the fidelity in terms of the OAM quadrature can be translated into the calculation of the fidelity in terms of the OAM quadrature of the probe state. According to the perturbed probe state after the atmospheric channel with density matrix Γ_{B_1} and the initial probe state before the channel with density matrix Γ_B , we can calculate its fidelity by [45,46]

$$F_{OAM} = \left[\text{Tr} \left\{ \sqrt{\sqrt{\Gamma_B} \Gamma_{B_1} \sqrt{\Gamma_B}} \right\} \right]^2. \tag{22}$$

For our scheme, the final output state of the entire system is measured by using the mode-matched balanced homodyne detection technology, so that the target state corre-

sponding to the detected state is pure with the assumption that the detection device is perfect. Therefore, this fidelity can be also expressed as

$$F_{OAM} = \text{Tr}[\Gamma_B \Gamma_{B_1}] = \langle \psi_{l,pr} | \Gamma_{B_1} | \psi_{l,pr} \rangle. \tag{23}$$

Therefore, the fidelity of the OAM multiplexed CV-QT system can be calculated as

$$F = F_{ap} \cdot F_{OAM}. \tag{24}$$

To illustrate the parallelism of the proposed OAM multiplexed free-space teleportation, we have done some simulations while changing the topological charge l carried by an initial probe state from -4 to 4 , the atmospheric refractive index structure parameter C_n^2 characterizing the turbulence intensity from $10^{-17} \text{ m}^{-2/3}$ to $10^{-13} \text{ m}^{-2/3}$, and the propagation distance z from 0 to 10 km , which are shown in Figure 6. The squeezing parameter r_s is set to 0.7 . The varying coloured surfaces represent the fidelity of free-space quantum teleportation with EPR entanglement for teleporting different OAM modes, whereas the light purple planes represent the fidelity of the classical limit [47]. The condition for a successful QT is that the fidelity of the teleportation is larger than the classical limit [22]. The results show that the fidelity exhibits monotonic attenuation as the atmospheric refractive index structure parameter C_n^2 and the propagation distance z increase, which means the difference between the output state after turbulence and the initial state is becoming larger and larger. This is because the turbulence causes crosstalk of OAM modes, leading to the spiral spectrum of OAM modes of the output state dramatically changing compared to that of the initial state. In addition, it is clear that, for the free-space QT with EPR entanglement carrying OAM, the larger the $|l|$ is, the lower the fidelity will be. This is because the inseparability of OAM-multiplexed entanglement source gets worse with the increase in $|l|$ [25]. Furthermore, the fidelity of the unknown input state in the case of weak turbulence and short distance can be better than that of the classical counterpart, thus establishing a dominant region of fidelity with respect to atmospheric turbulence intensity and transmission distance, as shown in the region to the left of the brown curve in the top projection of the figures.

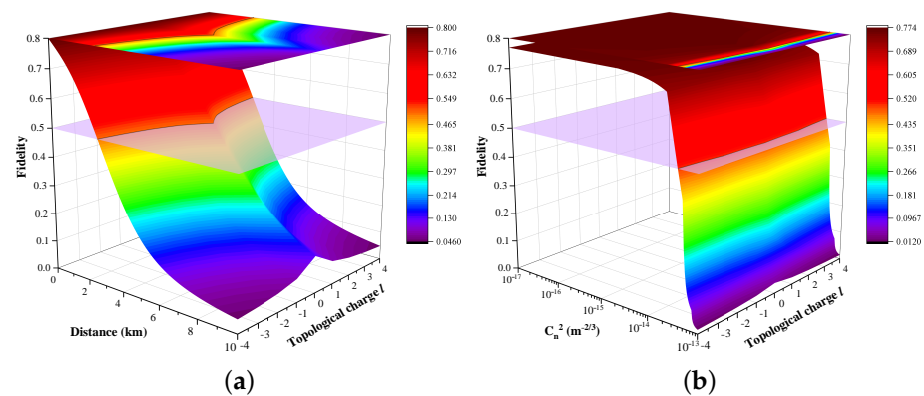


Figure 6. Fidelity of the proposed CV-QT protocol versus the topological charge number carried by the unknown input state and (a) the propagation distance; (b) the atmospheric turbulence intensity.

To reveal the superiority of the proposed OAM multiplexed free-space QT in terms of increasing the information transmission capacity, we assume that the unknown input state is an OAM superposition mode coded coherent state, which can be noted as $\rho_{in} = \sum_{x=-1}^l (\psi_{x,in} + \psi_{-x,in})$. The total number of the OAM modes is $N = 2l$. If the fundamental mode, i.e., the Gaussian mode, is also taken into account, then $N = 2l + 1$. Existing investigations have shown that the OAM superposition mode carried by input coherent state remains unchanged after the channel propagation, and the fidelity for teleporting $\rho'_{in} = \psi_{x,in} + \psi_{-x,in}$ is same as the one for teleporting $\psi_{x,in}$ ($\psi_{-x,in}$) because the squeezing

levels of EPR entanglement for these two cases are equal [25,27]. All of these indicate that we can construct OAM multiplexed channels of parallel quantum teleportation with fidelities beating the classical limit.

3.2. Channel Capacity

We further analyse the influence of transmission distance and atmospheric turbulence intensity on the channel capacity of the system, which can be defined as [35,48]

$$C = \max[H(n) - H(n|m)]$$

$$= \max_{\{P(n)\}} \left[- \sum_n P(n) \log_2 P(n) + \sum_n P(n) \sum_m P(m|n) \log_2 P(m|n) \right], \tag{25}$$

where $H(n)$ is the entropy of the initial probe state $|\psi_{n,pr}\rangle$, $H(n|m)$ is the conditional entropy of the sent state $|\psi_{n,pr}\rangle$ given the received state $|\psi_{m,pr}\rangle$, $P(n)$ is the probability of sending state $|\psi_{n,pr}\rangle$, and $P(m|n)$ is the conditional probability of receiving state $|\psi_{m,pr}\rangle$ under the condition of sending state $|\psi_{n,pr}\rangle$. In our scheme, different states are prepared with equal probability, so $P(n) = 1/N$.

The simulation results of the channel capacity with different numbers of OAM modes multiplexed in a weak Kolmogorov turbulence environment is shown in Figure 7. It can be seen from the figure that the channel capacity can be improved by increasing the number of multiplexed OAM modes, but this improvement trend gradually weakens as the number of modes continues to increase. For a system with $N = 2$, the channel capacity is reduced to below that for an ideal binary state channel when the transmission distance and the intensity of atmospheric turbulence increase to a certain level. Moreover, we also find that the channel capacity gradually decreases with the increase in transmission distance and the strengthening of turbulence intensity, which is attributed to the increase in the turbulent aberrations. These demonstrate that the channel capacity of the free-space QT system can be extended by means of OAM mode multiplexing.

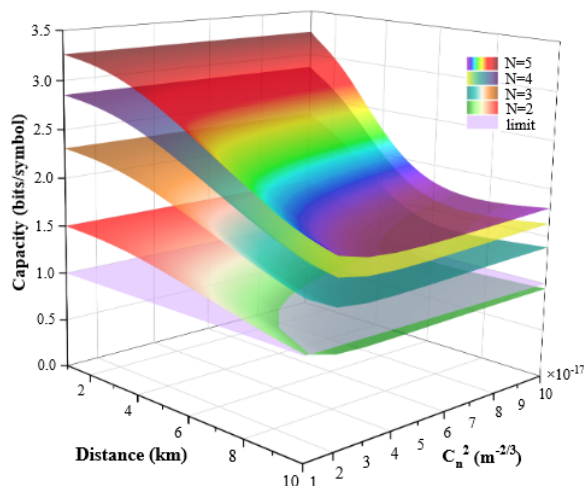


Figure 7. Channel capacity of the system with different numbers of OAM modes multiplexed versus the transmission distance and the atmospheric turbulence intensity. The purple plane represents the limit for the polarized codes.

4. Conclusions

In summary, we have proposed a scheme that utilizes the SFWM effect occurring within a hot ^{85}Rb vapor cell to prepare EPR entangled pairs carrying OAM for QT in a Kolmogorov-type atmospheric turbulence channel. The Bell-state measurement and the detection for the output state of the system employ the OAM mode-matched balanced homodyne detection technique, ensuring the teleportation of the unknown input quantum

state. The coherence between the probe and conjugate modes is shown to be weakened with the increase in transmission distance and atmospheric turbulence intensity, but it always exists, ensuring that the quantum states are not damaged under the considered conditions, ruling out the influence of decoherence effects on the system performance. Simulation results show that the proposed scheme can establish a region of superiority with respect to fidelity in the case of short distance and weak turbulence compared with the classical limit, and that it can significantly increase the channel capacity of the system through the multiplexing of the OAM carried by the EPR states compared with the limit for the polarized codes. Additionally, we can also conclude that the fidelity and channel capacity of the system decreases with the increase in the transmission distance and the intensity of the atmospheric turbulence, which points the way for further work to focus on mitigating the effects of atmospheric turbulence disturbances on system performance.

Author Contributions: Conceptualization, X.R. and H.Z.; methodology, S.X.; software, W.P. and H.X.; validation, X.R. and W.Z.; formal analysis, H.Z.; investigation, X.R.; resources, W.Z.; data curation, Y.Z.; writing—original draft preparation, X.R.; writing—review and editing, W.Z. and S.X.; visualization, S.X.; supervision, W.Z.; project administration, H.Z.; funding acquisition, H.Z. and X.R. All authors have read and agreed to the published version of the manuscript.

Funding: This work was supported by the Natural Science Foundation of Hunan Province (Grant No. 2021JJ30878), the Key Research and Development Program of Hunan Province (Grant Nos. 2020GK4063, 2022GK2016), the Key Project of Scientific Research of Hunan Provincial Education Department (Grant No. 22A0669), and the Fundamental Research Funds for the Central Universities of Central South University (Grant No. 2023ZZTS0362).

Institutional Review Board Statement: Not applicable.

Informed Consent Statement: Not applicable.

Data Availability Statement: Data are contained within the article.

Acknowledgments: We acknowledge the support from the Optoelectronic Information Center of Central South University.

Conflicts of Interest: The authors declare no conflict of interest.

Appendix A. Preparation for the OAM Multiplexed CV EPR States

The generation of the OAM multiplexed CV EPR states is shown in Figure A1a. A Gaussian beam is seeded into a warm ^{85}Rb vapor cell, serving as the pump beam of the SFWM process in the cell for generating OAM multiplexed EPR entangled pairs [27]. The energy level diagram utilized in this process is a double- Λ configuration as shown in Figure A1b, where two pump photons are converted into a conjugate and a probe photon. Because the pump beam does not carry OAM and the OAM is conserved during the SFWM process, the topological charges of the probe field $LG_{l,pr}$ and conjugate field $LG_{-l,conj}$ are opposite, which are depicted by the corresponding dashed line in the OAM spectrum shown in Figure A1c. The interaction Hamiltonian of the SFWM process can be expressed as [27,43]

$$\hat{H} = \sum_l i\hbar\gamma_l \hat{b}_{l,pr}^\dagger \hat{b}_{-l,conj}^\dagger + H.c, \quad (\text{A1})$$

where $\hat{b}_{l,pr}^\dagger$ and $\hat{b}_{-l,conj}^\dagger$ are the creation operators related to OAM modes of the probe and conjugate fields, respectively; \hbar is the Planck constant, l is the topological charge, γ_l is a constant characterizing the interaction strength of each OAM pair, and $H.c$ is the Hermitian conjugate.

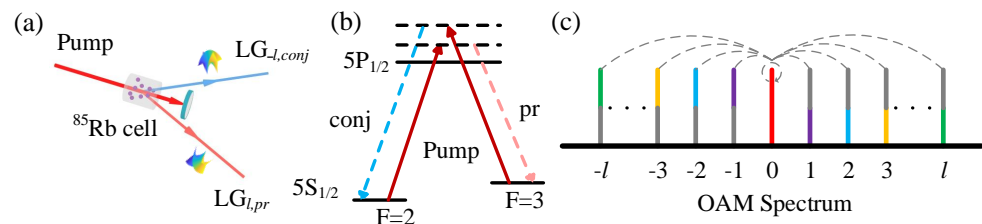


Figure A1. The generation of the OAM multiplexed CV EPR states. (a) The SFWM process occurs in a hot ⁸⁵Rb vapor cell for generating multiple pairs of OAM modes. (b) Double-Λ energy level diagram of ⁸⁵Rb D1 line in the SFWM process. (c) OAM spectrum from the SFWM process. pr, probe beam; conj, conjugate beam.

The output state of this process can be expressed as

$$|\Psi\rangle_{AB} = |\Psi\rangle_{-l} \otimes \dots \otimes |\Psi\rangle_0 \otimes \dots \otimes |\Psi\rangle_l, \tag{A2}$$

where $|\Psi\rangle_l = |\psi_{l,pr}, \psi_{-l,conj}\rangle$ presents a series of independent OAM multiplexed CV EPR entangled pairs generated in the SFWM process; $|\psi_{l,pr}\rangle$ and $|\psi_{-l,conj}\rangle$ represent the probe and conjugate modes carrying topological charge l and $-l$, respectively. Each pair of generated OAM multiplexed EPR modes can be described by corresponding amplitude and phase quadratures, namely [49]

$$\begin{aligned} \hat{X}_{l,pr} &= \frac{\hat{b}_{l,pr} + \hat{b}_{l,pr}^\dagger}{\sqrt{2}}, \hat{Y}_{l,pr} = \frac{\hat{b}_{l,pr} - \hat{b}_{l,pr}^\dagger}{\sqrt{2}i}, \\ \hat{X}_{-l,conj} &= \frac{\hat{b}_{-l,conj} + \hat{b}_{-l,conj}^\dagger}{\sqrt{2}}, \hat{Y}_{-l,conj} = \frac{\hat{b}_{-l,conj} - \hat{b}_{-l,conj}^\dagger}{\sqrt{2}i}. \end{aligned} \tag{A3}$$

Appendix B. Mode-Matched Balanced Homodyne Detection for OAM

In CV communication systems, the balanced homodyne detection (BHD) technique has proven to be an effective mode selection method, which allows the projection of the signal field modes onto an appropriately shaped local oscillator (LO), thus enabling mode selection and measurement. With this benefit, in our scheme, we also consider the use of the BHD technique for the selection and measurement of OAM modes in the signal field, with the implementation mechanism described below.

The schematic of BHD for OAM modes is shown in Figure A2. A signal field $\hat{a}e^{il_1\theta}$ with topological charge l_1 and a LO field $\hat{b}e^{il_2\theta}$ with topological charge l_2 interfere via a 50:50 beam splitter, outputting

$$\begin{aligned} \hat{c} &= \frac{1}{\sqrt{2}}[\hat{b}e^{il_2\theta} \cdot e^{i\phi} + \hat{a}e^{-il_1\theta}], \\ \hat{d} &= \frac{1}{\sqrt{2}}[\hat{b}e^{-il_2\theta} \cdot e^{i\phi} - \hat{a}e^{il_1\theta}], \end{aligned} \tag{A4}$$

where ϕ is the relative phase difference between the LO and the signal field. The two output fields are measured by photo detectors, and the photocurrent is then subtracted by a subtractor to obtain the current difference [27]

$$\begin{aligned} I &= \int_0^{2\pi} (\hat{c}^\dagger c - \hat{d}^\dagger d) d\theta \\ &= \int_0^{2\pi} \frac{1}{2} [\hat{b}^\dagger \hat{a} e^{-i(l_1+l_2)\theta} e^{-i\phi} + \hat{a}^\dagger \hat{b} e^{i(l_1+l_2)\theta} e^{i\phi} + \hat{b}^\dagger \hat{a} e^{i(l_1+l_2)\theta} e^{-i\phi} + \hat{a}^\dagger \hat{b} e^{-i(l_1+l_2)\theta} e^{i\phi}] d\theta. \end{aligned} \tag{A5}$$

As for the amplitude of the signal and the LO fields, there are

$$\hat{a} \approx |\alpha| + \delta\hat{a}, \hat{b} \approx |\beta| + \delta\hat{b}, \tag{A6}$$

where $\delta\hat{a}$ and $\delta\hat{b}$ represent the error. Without loss of generality, the intensity of the LO is much larger than that of the signal light, i.e., $|\beta| \gg |\alpha|$, thus all terms without $|\beta|$ in Equation (A5) can be ignored. Based on these, we can simplify the photocurrent I as

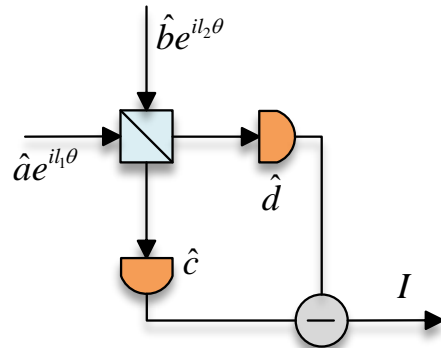


Figure A2. The schematic of BHD for OAM modes: l is the topological charge carried by the OAM modes, θ is the azimuthal angle.

$$I \propto \begin{cases} \int_0^{2\pi} |\beta| \cos[(l_1 + l_2)\theta] \delta X_a^\phi d\theta = 2\pi |\beta| \delta X_a^\phi, & l_1 = -l_2 \\ 0, & l_1 \neq -l_2 \end{cases} \tag{A7}$$

where $\delta X_a^\phi = \delta a e^{-i\phi} + \delta \hat{a}^\dagger e^{i\phi}$ is the quadrature amplitude of the signal field. From this equation, we can know that only the signal field carrying the opposite topological charge with LO can be detected.

In our scheme, the OAM mode-matched BHD is utilized by both the transmitter and the receiver. At the transmitter’s side, there are two BHDs used in the Bell-state measurement process for measuring the amplitude and phase quadratures of the input signals, respectively, which are the interference output of a balanced BS, with the following form

$$\begin{aligned} C &= (|\psi_{x,in}\rangle - |\psi_{-l,conj}\rangle) / \sqrt{2}, \\ D &= i(|\psi_{x,in}\rangle + |\psi_{-l,conj}\rangle) / \sqrt{2}, \end{aligned} \tag{A8}$$

where $|\psi_{x,in}\rangle$ and $|\psi_{-l,conj}\rangle$ are the unknown input state and the conjugate modes of the prepared EPR entangled states. The LO for the BHDs is obtained from the SLM modulated beam reversed by a Dove prism, which has a opposite topological charge with the unknown input state and can be denoted as $LG_{-x,LO}$. From the previous analysis, it is clear that C and D can be detected correctly only if they have a single topological charge opposite with LO. This also means that in the conjugate mode $|\psi_{-l,conj}\rangle$, the mode with $-l = x$ can be detected. Switching to another perspective, we can also generalize the topological charge x of the unknown input state to $-l$, in which case LO carries a topological charge of l . The measurement results of BHDs are

$$\begin{aligned} \hat{X}_- &= (\hat{X}_{-l,in} - \hat{X}_{-l,conj}) / \sqrt{2}, \\ \hat{Y}_+ &= (\hat{Y}_{-l,in} + \hat{Y}_{-l,conj}) / \sqrt{2}, \end{aligned} \tag{A9}$$

where \hat{X} and \hat{Y} represent the amplitude and phase quadrature.

As described in the displacement process in Section 2.1, the input signal of the two BHDs at the receiver’s side has the topological charge of $-l$, and the initial LO obtained by SLM modulation has a topological charge of $-l$. In order to enable the BHDs to work properly, a Dove prism is employed to reverse the topological charge of the initial LO.

Appendix C. Kolmogorov Turbulence Model

The modern atmospheric turbulence theory is based on the large Reynolds number turbulence theory proposed by Kolmogorov [50], which suggests that when the Reynolds number is large, turbulence will exhibit characteristic scale-free properties, i.e., it can be seen as consisting of a number of widely varying vortices of different scales. Specifically, the change in the mean velocity of the turbulence allows the largest vortex to gain energy, which is then transferred to smaller vortices, which break up into smaller vortices, and so on, with the energy being dissipated by viscosity in the smallest scale vortex. In this process, the large scale turbulence is anisotropic, whereas the small scale turbulence is isotropic and will eventually reach a state of statistical equilibrium with a universal statistical law.

According to the Kolmogorov turbulence theory, the scale of turbulence can be characterized by the turbulent outer scale l_{out} and the turbulent inner scale l_{in} . Therefore, the turbulence can be divided into three regions according to the level of the turbulent scale r , namely the energy-bearing region ($r > l_{out}$), the inertial region ($l_{in} < r < l_{out}$), and the dissipative region ($r < l_{in}$). In the energy-bearing region, the turbulence receives energy from the outside with anisotropy and transfers energy to the inertial region. In the inertial region, the viscous dissipation is less than the momentum of the turbulent vortex and the turbulence is isotropic. In the dissipative region, the viscous dissipation is greater than the momentum, resulting in less energy.

For the conventional Kolmogorov spectrum with the assumption of $l_{out} \rightarrow \infty$ and $l_{in} = 0$, we only need to consider the inertial region, where the refractive index structure function $D(r)$ is proportional to $r^{2/3}$, i.e.,

$$D(r) = C_n^2 r^{2/3}, \quad (\text{A10})$$

where C_n^2 is the atmospheric refractive index structure parameter. The power spectral density in this region can be expressed as

$$\Phi(\kappa) = \frac{1}{4\pi^2\kappa^2} \int_0^\infty \frac{\sin(\kappa r)}{\kappa r} \frac{d}{dr} \left[r^2 \frac{d}{dr} D(r) \right], \quad (\text{A11})$$

where κ is the magnitude of the three-dimensional coordinate vector in the Fourier domain. Substituting Equation (A10) into Equation (A11) yields the Kolmogorov spectrum as

$$\Phi(\kappa) = 0.033 C_n^2 \kappa^{-11/3}. \quad (\text{A12})$$

References

- Bennett, B.; Crepeau, J.; Peres, W. Teleporting an unknown quantum state via dual classical and Einstein-Podolsky-Rosen channels. *Phys. Rev. Lett.* **1993**, *70*, 1895–1899. [[CrossRef](#)] [[PubMed](#)]
- Vaidman, L. Teleportation of quantum states. *Phys. Rev. A* **1994**, *49*, 1473–1476. [[CrossRef](#)] [[PubMed](#)]
- Bouwmeester, D.; Pan, J.W.; Mattle, K.; Eibl, M.; Weinfurter, H.; Zeilinger, A. Experimental quantum teleportation. *Nature* **1997**, *390*, 575–579. [[CrossRef](#)]
- Boschi, D.; Branca, S.; De Martini, F.; Hardy, L.; Popescu, S. Experimental realization of teleporting an unknown pure quantum state via dual classical and Einstein-Podolsky-Rosen channels. *Phys. Rev. Lett.* **1998**, *80*, 1121–1125. [[CrossRef](#)]
- Marcikic, I.; de Riedmatten, H.; Tittel, W.; Zbinden, H.; Gisin, N. Long-distance teleportation of qubits at telecommunication wavelengths. *Nature* **2003**, *421*, 509–513. [[CrossRef](#)]
- Yin, J.; Ren, J.G.; Lu, H.; Cao, Y.; Yong, H.L.; Wu, Y.P.; Liu, C.; Liao, S.K.; Zhou, F.; Jiang, Y.; et al. Quantum teleportation and entanglement distribution over 100-kilometre free-space channels. *Nature* **2012**, *488*, 185–188. [[CrossRef](#)]
- Ma, X.S.; Herbst, T.; Scheidl, T.; Wang, D.Q.; Kropatschek, S.; Naylor, W.; Wittmann, B.; Mech, A.; Kofler, J.; Anisimova, E.; et al. Quantum teleportation over 143 kilometres using active feed-forward. *Nature* **2012**, *489*, 269–273. [[CrossRef](#)]
- Ren, J.G.; Xu, P.; Yong, H.L.; Zhang, L.; Liao, S.K.; Yin, J.; Liu, W.Y.; Cai, W.Q.; Yang, M.; Li, L.; et al. Ground-to-satellite quantum teleportation. *Nature* **2017**, *549*, 70–73. [[CrossRef](#)]
- Huo, M.; Qin, J.L.; Cheng, J.L.; Yan, Z.H.; Qin, Z.Z.; Su, X.L.; Jia, X.J.; Xie, C.D.; Peng, K.C. Deterministic quantum teleportation through fiber channels. *Sci. Adv.* **2018**, *4*, 1–7. [[CrossRef](#)]
- Braunstein, S.L.; Kimble, H.J. Teleportation of continuous quantum variables. *Phys. Rev. Lett.* **1998**, *80*, 869–872. [[CrossRef](#)]
- Furusawa, A.; Sorensen, J.L.; Braunstein, S.L.; Fuchs, C.A.; Kimble, H.J.; Polzik, E.S. Unconditional quantum teleportation. *Science* **1998**, *282*, 706–709. [[CrossRef](#)]

12. Yang, Y.; Li, F.L. Entanglement properties of non-Gaussian resources generated via photon subtraction and addition and continuous-variable quantum-teleportation improvement. *Phys. Rev. A* **2009**, *80*, 022315. [[CrossRef](#)]
13. Jiang, K.X. The role of the non-Gaussianity plays in the enhancement of the fidelity in continuous variable quantum teleportation. *Opt. Commun.* **2013**, *300*, 286–292. [[CrossRef](#)]
14. Wen, Z.N.; Yi, Y.G.; Xu, X.W.; Guo, Y. Continuous-variable quantum teleportation with entanglement enabled via photon catalysis. *Quantum Inf. Process.* **2022**, *21*, 325. [[CrossRef](#)]
15. Wen, Z.N.; Yi, Y.G.; Xu, X.W.; Guo, Y. Continuous variable quantum teleportation with noiseless linear amplifier. *Acta Phys. Sin.* **2022**, *71*, 130307. [[CrossRef](#)]
16. Fiurášek, J. Teleportation-based noiseless quantum amplification of coherent states of light. *Opt. Express* **2022**, *30*, 1466–1489. [[CrossRef](#)]
17. Wu, H.; Liu, X.; Zhang, H.; Ruan, X.C.; Guo, Y. Performance analysis of continuous variable quantum teleportation with noiseless linear amplifier in seawater channel. *Symmetry-Basel* **2022**, *14*, 997. [[CrossRef](#)]
18. Xu, J.Y.; Xu, X.W.; Zuo, Z.Y.; Guo, Y. Continuous variable quantum teleportation through turbulent channels. *Phys. Scr.* **2022**, *97*, 045103. [[CrossRef](#)]
19. Andersen, U.L.; Ralph, T.C. High-fidelity teleportation of continuous-variable quantum states using delocalized single photons. *Phys. Rev. Lett.* **2013**, *111*, 050504. [[CrossRef](#)]
20. Marshall, K.; James, D.F.V. High-fidelity teleportation of continuous-variable quantum states with discrete-variable resources. *J. Opt. Soc. Am. B* **2014**, *31*, 423–428. [[CrossRef](#)]
21. Pyrkov, A.N.; Byrnes, T. Quantum teleportation of spin coherent states: Beyond continuous variables teleportation. *New J. Phys.* **2014**, *16*, 073038. [[CrossRef](#)]
22. Zubarev, A.; Cuzminschi, M.; Isar, A. Continuous variable quantum teleportation of a thermal state in a thermal environment. *Results Phys.* **2022**, *39*, 105700. [[CrossRef](#)]
23. Zhao, H.; Feng, J.X.; Sun, J.K.; Li, Y.J.; Zhang, K.S. Real time deterministic quantum teleportation over 10 km of single optical fiber channel. *Opt. Express* **2022**, *30*, 3770–3782. [[CrossRef](#)]
24. Zuo, Z.Y.; Wang, Y.J.; Liao, Q.; Guo, Y. Overcoming the uplink limit of satellite-based quantum communication with deterministic quantum teleportation. *Phys. Rev. A* **2021**, *104*, 022615. [[CrossRef](#)]
25. Liu, S.S.; Lou, Y.B.; Jing, J.T. Orbital angular momentum multiplexed deterministic all-optical quantum teleportation. *Nat. Commun.* **2020**, *11*, 3875. [[CrossRef](#)] [[PubMed](#)]
26. Wu, Y.M.; Wang, Q.W.; Tian, L.; Zhang, X.L.; Wang, J.W.; Shi, S.P.; Wang, Y.J.; Zheng, Y.H. Multi-channel multiplexing quantum teleportation based on the entangled sideband modes. *Photon. Res.* **2022**, *10*, 1909–1914. [[CrossRef](#)]
27. Pan, X.Z.; Yu, S.; Zhou, Y.F.; Zhang, K.; Zhang, K.; Lv, S.C.; Li, S.J.; Wang, W.; Jing, J.T. Orbital-angular-momentum multiplexed continuous-variable entanglement from four-wave mixing in hot atomic vapor. *Phys. Rev. Lett.* **2019**, *123*, 070506. [[CrossRef](#)]
28. Kogelnik, H.; Li, T. Laser beams and resonators. *Appl. Opt.* **1966**, *5*, 1550–1567. [[CrossRef](#)]
29. Allen, L.; Beijersbergen, M.W.; Spreeuw, R.J.C.; Woerdman, J.P. Orbital angular momentum of light and the transformation of Laguerre-Gaussian laser modes. *Phys. Rev. A* **1992**, *45*, 8185–8189. [[CrossRef](#)]
30. Wang, Z.Q.; Malaney, R.; Burnett, B. Satellite-to-earth quantum key distribution via orbital angular momentum. *Phys. Rev. Appl.* **2020**, *14*, 064031. [[CrossRef](#)]
31. Ruan, X.C.; Zhang, H.; Zhao, W.; Jin, D.; Wang, Z.P.; Guo, Y. Orbital angular momentum-encoded quantum digital signature over atmospheric channel. *Quantum Inf. Process.* **2022**, *21*, 191. [[CrossRef](#)]
32. van Loock, P.; Braunstein, S.L. Multipartite entanglement for continuous variables: A quantum teleportation network. *Phys. Rev. Lett.* **2000**, *84*, 3482–3485. [[CrossRef](#)] [[PubMed](#)]
33. Ibrahim, A.H.; Roux, F.S.; McLaren, M.; Konrad, T.; Forbes, A. Orbital-angular-momentum entanglement in turbulence. *Phys. Rev. A* **2013**, *88*, 012312. [[CrossRef](#)]
34. Hu, Z.D.; Zhu, Y.; Wang, J.C. Quantum coherence of thermal biphoton orbital angular momentum state and its distribution in non-Kolmogorov atmospheric turbulence. *Opt. Express* **2022**, *30*, 20185–20193. [[CrossRef](#)] [[PubMed](#)]
35. Paterson, C. Atmospheric turbulence and orbital angular momentum of single photons for optical communication. *Phys. Rev. Lett.* **2005**, *94*, 153901. [[CrossRef](#)]
36. Tyler, G.A.; Boyd, R.W. Influence of atmospheric turbulence on the propagation of quantum states of light carrying orbital angular momentum. *Opt. Lett.* **2009**, *34*, 142–144. [[CrossRef](#)]
37. Wang, X.Y.; Zhao, S.H.; Dong, C.; Zhu, Z.D.; Gu, W.Y. Orbital angular momentum-encoded measurement device independent quantum key distribution under atmospheric turbulence. *Quantum Inf. Process.* **2019**, *18*, 304. [[CrossRef](#)]
38. Ruan, X.C.; Shi, W.H.; Chen, G.J.; Zhao, W.; Zhang, H.; Guo, Y. High-rate continuous-variable quantum key distribution with orbital angular momentum multiplexing. *Entropy* **2021**, *23*, 1187. [[CrossRef](#)]
39. Ricklin, J.C.; Hammel, S.M.; Eaton, F.D.; Lachinova, S.L. Atmospheric channel effects on free-space laser communication. *J. Opt. Fiber. Commun. Rep.* **2006**, *3*, 111–158. [[CrossRef](#)]
40. Wang, S.Y.; Huang, P.; Wang, T.; Zeng, G.H. Feasibility of all-day quantum communication with coherent detection. *Phys. Rev. Appl.* **2019**, *12*, 024041. [[CrossRef](#)]

41. Laudenbach, F.; Pacher, C.; Fung, C.H.F.; Poppe, A.; Peev, M.; Schrenk, B.; Hentschel, M.; Walther, P.; Hubel, H. Continuous-variable quantum key distribution with Gaussian modulation—The theory of practical implementations. *Adv. Quantum Technol.* **2018**, *1*, 1800011. [[CrossRef](#)]
42. Kish, S.P.; Villaseñor, E.; Malaney, R.; Mudge, K.A.; Grant, K.J. Feasibility assessment for practical continuous variable quantum key distribution over the satellite-to-Earth channel. *Quantum Eng.* **2020**, *2*, e50. [[CrossRef](#)]
43. Wen, H.; Zeng, L.; Ma, R.; Kang, H.J.; Liu, J.; Qin, Z.Z.; Su, X.L. Quantum coherence of an orbital angular momentum multiplexed continuous-variable entangled state. *Opt. Contin.* **2022**, *1*, 697–704. [[CrossRef](#)]
44. Baumgratz, T.; Cramer, M.; Plenio, M.B. Quantifying coherence. *Phys. Rev. Lett.* **2014**, *113*, 140401. [[CrossRef](#)] [[PubMed](#)]
45. Liu, J.; Nape, I.; Wang, Q.K.; Valles, A.; Wang, J.; Forbes, A. Multidimensional entanglement transport through single-mode fiber. *Sci. Adv.* **2020**, *6*, eaay0837. [[CrossRef](#)]
46. Ndagano, B.; Perez-Garcia, B.; Roux, F.S.; McLaren, M.; Rosales-Guzman, C.; Zhang, Y.W.; Mouane, O.; Hernandez-Aranda, R.I.; Konrad, T.; Forbes, A. Characterizing quantum channels with non-separable states of classical light. *Nat. Phys.* **2017**, *13*, 397–402. [[CrossRef](#)]
47. Braunstein, S.L.; Fuchs, C.A.; Kimble, H.J.; van Loock, P. Quantum versus classical domains for teleportation with continuous variables. *Phys. Rev. A* **2001**, *64*, 022321. [[CrossRef](#)]
48. Malik, M.; O’Sullivan, M.; Rodenburg, B.; Mirhosseini, M.; Leach, J.; Lavery, M.P.J.; Padgett, M.J.; Boyd, R.W. Influence of atmospheric turbulence on optical communications using orbital angular momentum for encoding. *Opt. Express* **2012**, *20*, 13195–13200. [[CrossRef](#)]
49. Wang, X.T.; Jing, J.T. Deterministic entanglement of large-scale Hermite-Gaussian modes. *Phys. Rev. Appl.* **2022**, *18*, 024057. [[CrossRef](#)]
50. Kolmogorov, A.N. The local structure of turbulence in incompressible viscous fluid for very large Reynolds numbers. *Proc. Roy. Soc. A-Math. Phys. Eng. Sci.* **1991**, *434*, 9–13.

Disclaimer/Publisher’s Note: The statements, opinions and data contained in all publications are solely those of the individual author(s) and contributor(s) and not of MDPI and/or the editor(s). MDPI and/or the editor(s) disclaim responsibility for any injury to people or property resulting from any ideas, methods, instructions or products referred to in the content.